

A Turbulence Model Sensitivity Analysis on the Hydraulic Behavior in the Inlet Plenum of the Proposed NIST Neutron Source Design

Abdullah G. Weiss, Joy S. Shen*, Anil Gurgent†
 NIST Center for Neutron Research
 100 Bureau Drive, Gaithersburg, MD 20899, USA
 abdullah.weiss@nist.gov; joy.shen@nist.gov; anil.gurgent@nist.gov

doi.org/10.13182/NURETH20-40168

ABSTRACT

The NIST Neutron Source, or NNS, is a proposed reactor designed to eventually replace the aging National Bureau of Standards Reactor at the NIST Center for Neutron Research (NCNR). The NNS is a light water moderated and cooled, compact reactor used to provide a reliable flux of cold and thermal neutrons for various neutron scattering and irradiation experiments. The reactor will be fueled with U-10Mo LEU curved plates, yielding flow channels that resemble those in other research reactors with plate-type fuels. This work focuses on assessing the flow behavior in the inlet plenum leading into the flow channels cooling the fuel plates, where a 2-dimensional representation of the inlet plenum is modeled using OpenFOAM®. The inlet plenum has a geometry that induces complex phenomena where the flow gets separated, then mixed, then separated again within a very short lead-in to the fuel plates, which necessitates the use of computational fluid dynamics or CFD models for further analyses. The geometry and mesh are discussed, and multiple Reynolds-Averaged Navier Stokes (RANS) models are investigated and compared including the standard $k-\epsilon$, standard $k-\omega$, $k-\omega$ SST, realizable $k-\epsilon$, and Spalart-Allmaras models. The resulting pressure and velocity distributions at the inlet of the fuel channels are computed for each of the RANS models, where the sensitivity of the results to variations in the models is discussed in detail. Comparisons to canonical flows from literature are made where appropriate to provide an insight on the validity of each model.

KEYWORDS

CFD; Turbulence; NNS; Sensitivity; RANS

1. INTRODUCTION

The National Institute of Standards and Technology (NIST) houses multiple research laboratories, including the NIST Center for Neutron Research (NCNR), where the National Bureau of Standards Reactor (NBSR) resides. The NBSR is a 20 MW_{th} heavy-water moderated and cooled research reactor that has been supplying thermal and cold neutrons to the international neutron physics community for

* Additional Affiliation: Department of Mechanical Engineering, University of Maryland, College Park, MD 20742, USA

† Additional affiliation: Department of Materials Science and Engineering, University of Maryland, College Park, MD 20742, USA

over 50 years. A recent effort by the NCNR explores a replacement for the NBSR to continue delivering neutrons for the scientific community and expand the neutron experimentation capabilities in the NCNR. The NIST Neutron Source (NNS) is the proposed replacement for the NBSR, and several efforts have been pursued toward its design and analysis [1-3]. A previous analysis [4] performed preliminary investigations on the NNS in-core flow behavior with simplified computational fluid dynamics (CFD) models. It was found that the inlet region preceding the fuel assemblies required additional characterization. This work focuses on inlet region characterization, where the resulting velocity and pressure behaviors are of most interest.

This work favors the utilization of Reynolds-Averaged Navier-Stokes (RANS) turbulence models for their convenience and relatively low computational costs. Multiple RANS models are applied, including $k-\epsilon$, $k-\omega$, $k-\omega$ SST, realizable $k-\epsilon$, and the Spalart-Allmaras. Results from each model are compared using spanwise traces of velocity and pressure to better illustrate the models' variations. All models in this work are developed using OpenFOAM code [5], specifically OpenFOAM version 9.

2. METHODOLOGY

The NNS preconceptual design consists of a 3x3 core, resulting in 9 total fuel assemblies, four reactivity safety blades and 2 reactivity control blades. A total of 21 curved fuel plates are found in each assembly, resulting in a total of 64 coolant channels in each row of the core, where an upwards forced convection flow of light-water is used as coolant and moderator in the core. Figure 1 illustrates the core geometry with a section view highlighting the coolant flow path in the core. Note how Figure 1 identifies 3 regions of interest: (1) the inlet region at the bottom of the geometry, (2) the active height where the fuel elements and coolant channels lie, and (3) the outlet region at the top of the shown geometry. The active height consists of an array of separated identical rectangular channels. Each channel in this region can be simulated by a single mesh and model by varying the inlet and boundary conditions based on the location of the coolant channel and its expected heating from neighboring fuel plate(s). The outlet region is a mixing plenum that does not require detailed analysis to ensure proper fuel cooling and safety in the core.

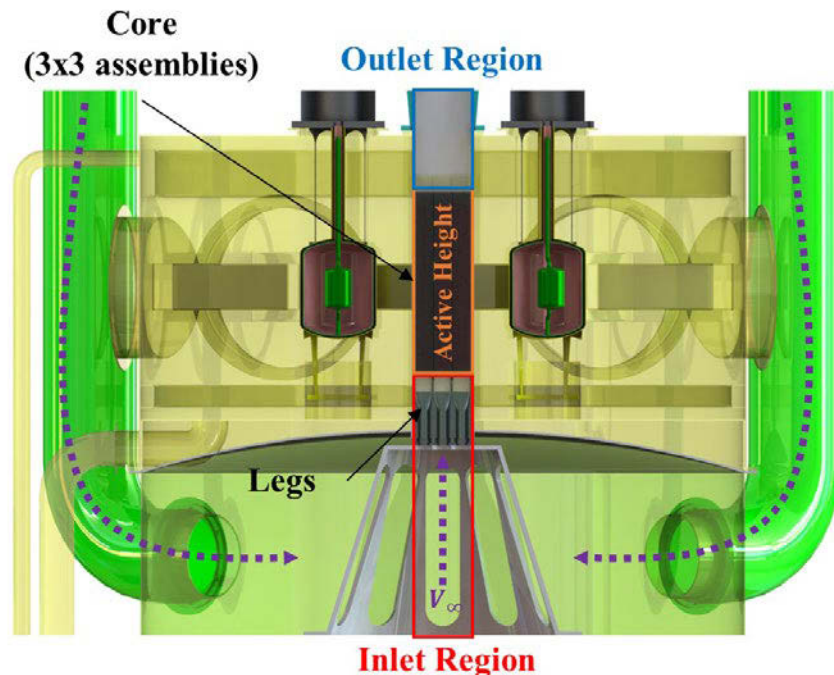


Figure 1. A section view of the NNS core showing its layout and the flow geometry.

Of most interest to this work is the inlet region, which is critical to understand the inlet behavior of each channel providing cooling to the fuel plates. Although the flow geometry is simple, the legs from the lower grid plate induce flow separation and downstream mixing prior to the final separation into each fuel assembly and each respective coolant channel. As such, the flow in the inlet region exhibits a separation-mixing-separation behavior that will yield concerns about adverse pressure gradients and considerable velocity gradients that may yield uneven flow distribution into the coolant channels. The uneven flow distribution is undesirable because certain fuel plates may not receive sufficient cooling. Based on literature on triple-channel mixing in rectangular geometries [6], it is anticipated that the center fuel assemblies will have lower velocities than the outer fuel assemblies, which yields a safety concern that may require a solution in future iterations of the design. To verify this concern, this work only models the inlet region using multiple RANS turbulence models.

2.1. Mesh Setup

A 2-dimensional representation of the inlet region is adopted per Figure 2, where a simple mesh convergence study is performed by increasing the number of elements until a streamwise velocity (V) solution converges to within $\sim 10^{-4}$ m/s in the standard $k-\epsilon$ model. The convergent mesh, shown in Figure 2, contains 48,140 hexahedral elements (97,920 nodes) with a maximum skewness of ~ 0.108 and a y^+ in the range of 0.05-250 near the walls. Higher y^+ values are used in the regions closest to the inlet of the region (at the bottom). At the legs, the y^+ varies between 0.05 and 0.25, persisting as the flow progresses toward the active height (top of the simulated geometry).

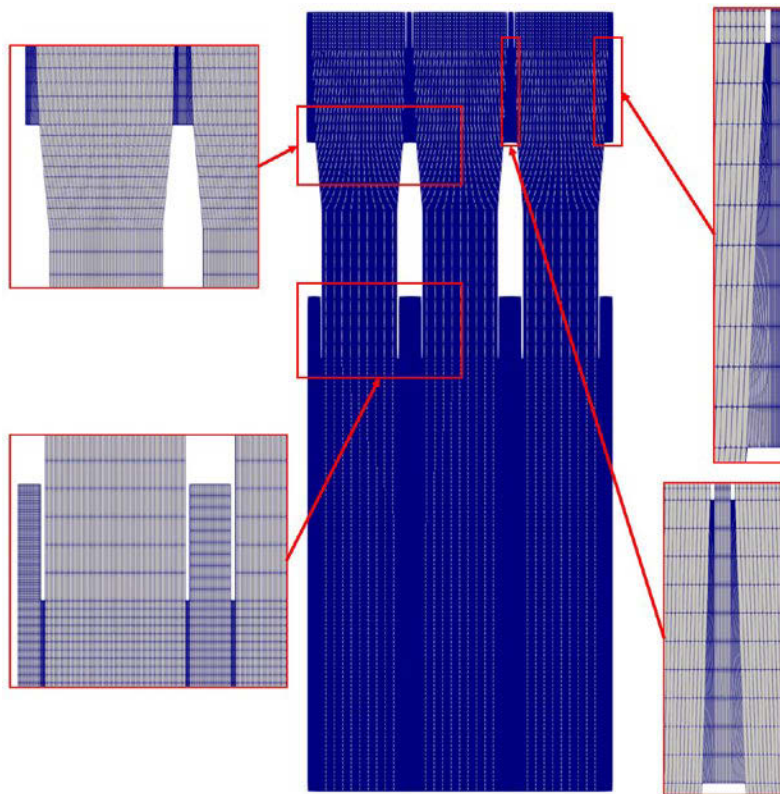


Figure 2. A view of the mesh utilized in this work for the 2-D representation of the inlet region.

Considering that the y^+ towards the top of the geometry is ~ 0.25 , it should be capable of capturing some physics on the scale of the viscous sublayer, but this study is not intended for such high fidelity

understanding of the flow. A higher fidelity turbulence modeling approach, such as Large Eddy Simulation (LES) models are considered more appropriate for characterizing the turbulent boundary layer behavior near the walls. It should also be noted that there is currently no need to accurately characterize the boundary layer in the inlet region, so it is likely that an LES model may not be necessary for the inlet region characterization; however, it would serve as a good verification of the RANS models adopted for this work. Additionally, it is likely advantageous to develop the RANS models in multiple CFD codes as an additional form of verification for the CFD solutions. To that end, a simultaneous effort is ongoing to also study how the velocities and pressure fields vary with varying RANS models using ANSYS® FLUENT [7], but a direct comparison between the codes is reserved to a future work.

2.2. Model Setup

The RANS models utilize the averaged forms of the Navier-Stokes equations shown in equations (1-2), where $\langle U_i \rangle$ represents the averaged form of any i -th component of the velocity and $\langle P \rangle$ is the averaged pressure. Note the dependence on the kinematic viscosity ν and the Reynolds stresses $\langle u_i u_j \rangle$, which can be expressed via the Boussinesq approximation shown in equation (3) [8-9]. Per the Boussinesq approximation, one also needs to compute the turbulent kinetic energy (k) and the turbulent viscosity (ν_t) in order to effectively close these sets of equations, which is where the distinctions between the RANS turbulence models arise.

$$\frac{\partial \langle U_i \rangle}{\partial t} + \langle U_j \rangle \frac{\partial \langle U_i \rangle}{\partial x_j} = -\frac{\partial \langle P \rangle}{\partial x_i} - \frac{\partial \langle u_i u_j \rangle}{\partial x_j} + \nu \frac{\partial^2 \langle U_i \rangle}{\partial x_j \partial x_j} \quad (1)$$

$$\frac{\partial^2 \langle P \rangle}{\partial x_j \partial x_j} = -2 \frac{\partial \langle U_i \rangle}{\partial x_j} \frac{\partial \langle U_j \rangle}{\partial x_i} - \frac{\partial^2 \langle u_i u_j \rangle}{\partial x_j \partial x_j} \quad (2)$$

$$\langle u_i u_j \rangle = \frac{2}{3} k \delta_{ij} - \nu_t \left(\frac{\partial \langle U_i \rangle}{\partial x_j} + \frac{\partial \langle U_j \rangle}{\partial x_i} \right) \quad (3)$$

The most common turbulence models are of the 2-equation kind like the k - ϵ standard model [10] represented by equations (4-5). In this model, k and its dissipation rate ϵ are modeled via their own transport equations which depend on model coefficients that can be found in Table I. In k - ϵ models it is possible to represent ν_t as a function of k , ϵ , and the model coefficient C_μ per equation (6). This model is very popular, particularly for industrial applications as it offers good conversion and low computational costs relative to other more sophisticated RANS models. It is important to note that standard k - ϵ is not meant for low Reynolds number (Re) flows, which naturally makes it struggle in modeling near-wall and boundary layer behavior.

$$\frac{\partial k}{\partial t} + \langle U_j \rangle \frac{\partial k}{\partial x_j} = -\langle u_i u_j \rangle \frac{\partial \langle U_i \rangle}{\partial x_j} - \epsilon + \frac{\partial}{\partial x_j} \left[\left(\nu + \frac{\nu_t}{\sigma_k} \right) \frac{\partial k}{\partial x_j} \right] \quad (4)$$

$$\frac{\partial \epsilon}{\partial t} + \langle U_j \rangle \frac{\partial \epsilon}{\partial x_j} = -C_{\epsilon 1} \frac{\epsilon}{k} \langle u_i u_j \rangle \frac{\partial \langle U_i \rangle}{\partial x_j} - C_{\epsilon 2} \frac{\epsilon^2}{k} + \frac{\partial}{\partial x_j} \left[\left(\nu + \frac{\nu_t}{\sigma_\epsilon} \right) \frac{\partial \epsilon}{\partial x_j} \right] \quad (5)$$

$$\nu_t = C_\mu \frac{k^2}{\epsilon} \quad (6)$$

Another well-known 2-equation RANS model is the k - ω model [11], which is shown in equations (7-8). This model is found to perform well for low Re flows, allowing it to model the near-wall behavior of flows notably better than the standard k - ϵ model. In this model, the ν_t can be represented as a function of the specific dissipation rate ω per equation (9). Note the similarities between k - ϵ and k - ω models, where β^* essentially substitutes C_μ in the k - ω model. The model constants for k - ω can be found in Table I.

$$\frac{\partial k}{\partial t} + \langle U_j \rangle \frac{\partial k}{\partial x_j} = -\langle u_i u_j \rangle \frac{\partial \langle U_i \rangle}{\partial x_j} - \beta^* k \omega + \frac{\partial}{\partial x_j} \left[\left(\nu + \nu_t \sigma^* \right) \frac{\partial k}{\partial x_j} \right] \quad (7)$$

$$\frac{\partial \omega}{\partial t} + \langle U_j \rangle \frac{\partial \omega}{\partial x_j} = -\alpha \frac{\omega}{k} \langle u_i u_j \rangle \frac{\partial \langle U_i \rangle}{\partial x_j} - \beta \omega^2 + \frac{\partial}{\partial x_j} \left[\left(\nu + \frac{\nu_t}{\sigma} \right) \frac{\partial \omega}{\partial x_j} \right] \quad (8)$$

$$v_t = \frac{k}{\omega} = \beta^* \frac{k^2}{\epsilon} \tag{9}$$

A 1-equation model that is popular for usage, particularly in low Re flows, is the Spalart-Allmaras (SA) model [12]. The SA model is a 1-equation v_t transport model of the form shown in equation (10), and it heavily depends on multiple constants, most of which can be found in Table I for the reader’s convenience. It is recommended that the reader refers to Spalart and Allmaras’s original work [12] for additional information on the model. It is important to note that the original model coefficients used by Spalart and Allmaras are also used in this work. The reader should also note that the Dacles-Mariani modification [13] is not used in this work.

$$\frac{\partial \tilde{v}}{\partial t} + \langle U_j \rangle \frac{\partial \tilde{v}}{\partial x_j} = -c_{b1} \tilde{S} \tilde{v} - c_{w1} f_w \left(\frac{\tilde{v}}{d}\right)^2 + \frac{1}{\sigma} \frac{\partial}{\partial x_k} \left[(\nu + \tilde{v}) \frac{\partial \tilde{v}}{\partial x_k} \right] + \frac{c_{b2}}{\sigma} \frac{\partial \tilde{v}}{\partial x_k} \frac{\partial \tilde{v}}{\partial x_k} \tag{10}$$

An additional two, relatively more sophisticated, models are used in this work, namely the k - ω Shear Stress Transport (SST) model [14] and the Realizable k - ϵ model [15], which will be referred to as SST and RKE hereafter, respectively. The SST model is a variant of standard k - ω that utilizes k - ω near the wall and standard k - ϵ in the freestream. This substitution between ϵ and ω near and away from the walls of a domain yield a cross-diffusion term between k and ω that uses a blending function to smoothen the transition between standard k - ω near the wall to standard k - ϵ in the freestream. Notably, the v_t is defined differently in the SST model and follows the formulation in equation (11), where it considers the influence of the shear stress component like the half-equation model of Johnson and King [16]. This accounting for the shear stress contributions improves the performance of the model for flows with strong adverse pressure gradients.

$$v_t = \frac{\alpha_1 k}{\max(\alpha_1 \omega, S F_2)}, \quad \begin{cases} \alpha_1 = \frac{5}{9} \\ F_2 = \tanh \left(\left[\max \left(\frac{2\sqrt{k}}{\beta^* \omega y}, \frac{500\nu}{y^2 \omega} \right) \right]^2 \right) \\ S = \frac{\omega}{k} \langle u_i u_j \rangle \frac{\partial \langle u_i \rangle}{\partial x_j} \end{cases} \tag{11}$$

The RKE model [15] reformulates equation (5) from the standard k - ϵ model and includes a dynamic treatment for C_μ to satisfy realizability of the $\langle u_i u_j \rangle$. These alteration from standard k - ϵ enable greater generalizability and makes the model applicable to significantly more complex flow phenomena. Notably, the dynamic adjustment of C_μ allows the model to become more sensitive to flow topology and improves the prediction of mean flow quantities [17]. The C_μ is computed per equation (12), which makes it a function of the shear velocity (U^*), and the unique model constants of A_0 and A_s . The A_s in particular depends on the shear stress ratio (W), which is discussed in greater detail in literature [18].

$$C_\mu = \frac{1}{A_0 + A_s \frac{k U^*}{\epsilon}}, \quad \begin{cases} A_0 = 4.04 \\ A_s = \sqrt{6} \cos \left(\frac{1}{3} \cos^{-1}(\sqrt{6} W) \right) \end{cases} \tag{12}$$

Table I. The model coefficients for multiple RANS models used in this work.

k - ϵ	C_μ	$C_{\epsilon 1}$	$C_{\epsilon 2}$	σ_k	σ_ϵ			
		0.09	1.44	1.92	1.0	1.3		
k - ω	β^*	α	β	σ^*	σ			
	0.09	0.5	0.075	0.5	0.5			
SA	C_{b1}	C_{b2}	C_{v1}	σ	C_{w1}	C_{w2}	C_{w3}	κ
	0.14	0.62	7.1	2/3	3.24	0.3	2.0	0.41

With the RANS models defined, it becomes relevant to consider the boundary conditions and any user inputs utilized in this work. Note that all inputs and boundary conditions are identical. The boundary conditions are all listed in Table II, where x_i represents any axis of motion. Note that since the coolant in the core is light water, the thermophysical properties were evaluated for water at atmospheric pressure and a temperature of 43.5 °C, which yields a density of $\rho = 990.8 \text{ kg/m}^3$ and a kinematic viscosity of $\nu = 6.19 \times 10^{-7} \text{ m}^2/\text{s}$. The hydraulic diameter is $D = 24.65 \text{ cm}$ (based on the inlet width in the simulated geometry), and the inlet velocity is $V_\infty = 12.78 \text{ m/s}$. A turbulence intensity of $T_i = 10\%$ is assumed, which enables the computation of bulk values of k , ϵ and ω (denoted by the subscript ∞) that can also be used at the inlet. Per equation (13), the bulk turbulent kinetic energy (k_∞) is computed as a function of the T_i and V_∞ , which then enables the computation of ϵ_∞ and ω_∞ per equations (6) and (9), respectively. The turbulent viscosity is assumed to be 15 times the ν ($\nu_{t,\infty} \sim 15\nu$).

$$k_\infty = \frac{3}{2}(T_i \cdot V_\infty) \tag{13}$$

Table II. The boundary conditions used in this work.

Variable	Inlet	Outlet	Walls
U	$U = 0$	$\frac{\partial U}{\partial x_i} = 0$	No Slip
V	V_∞	$\frac{\partial V}{\partial x_i} = 0$	No Slip
P	$\frac{\partial P}{\partial x_i} = 0$	$P = 0$	$\frac{\partial P}{\partial x_i} = 0$
k	k_∞	$\frac{\partial k}{\partial x_i} = 0$	$\frac{\partial k}{\partial x_i} = 0$
ϵ, ω	$\epsilon_\infty, \omega_\infty$	$\frac{\partial \{\epsilon, \omega\}}{\partial x_i} = 0$	Wall function
ν_t	$\nu_{t,\infty}$	$\nu_{t,\infty}$	Wall function

Note that wall functions are used for ω , ϵ , and ν_t to calculate their values at the wall. The ω and ϵ values at the wall are computed based on the average of their values in neighboring cells. The ν_t wall function dictates its wall value based on the k and y^+ , where the ν_t is set to zero when the cell reaches the intersection between the viscous and logarithmic sublayers in the turbulent boundary layer. It is also important to note the adoption of the popular convention for velocity components, where U is the horizontal velocity and V is the vertical velocity. The results are non-dimensionalized in this work for greater generalizability for the reader, where either of the velocity components are made unitless by dividing them with V_∞ . The P is made non-dimensional by dividing it with the dynamic pressure at the inlet, which yields the coefficient of pressure (C_p) per equation (14).

$$C_p = \frac{2P}{\rho V_\infty^2} \tag{14}$$

3. Results

The resulting spatial evolution of the non-dimensionalized parameters computed from each model are discussed in this section. This work only discusses the spatial evolution of the non-dimensionalized streamwise velocity (V/V_∞), the non-dimensionalized spanwise velocity (U/V_∞), and the C_p . The total fields are shown for each model and enable a quick comparison study between the models. Additionally, to enable a more quantitative discussion, spanwise profiles of the metrics are shown for each of the

models alongside a set of statistics that can help understand the variability between them. The streamwise profiles are taken at multiple streamwise locations (Y/D) as visualized in Figure 3 and listed in Table III.

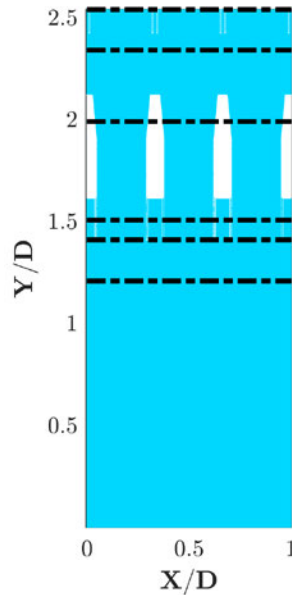


Figure 3. The streamwise trace locations considered for this work's spanwise profiles.

Table III. The streamwise locations considered for the spanwise profiles.

Trace	Y/D	Description
1	1.2	Directly upstream of separation from legs
2	1.4	Start of separation
3	1.5	Directly downstream of separation
4	2	Directly upstream of mixing
5	2.3	$\sim 0.15 Y/D$ into the mixing
6	2.5	Directly upstream of active height

3.1. Streamwise Velocity

Figure 4 shows the V/V_∞ fields for each of the investigated models in this work. Note that all of the models are initialized with a zero-velocity and zero-pressure field at the first iteration, with the exception of the "Initialized Realizable $k-\epsilon$ " case shown in Figure 4 where the model was initialized with the bulk velocity such that $V = V_\infty$ everywhere (except for the boundaries) at the first iteration. This is a notable distinction because the RKE model in-particular is the only one that yielded two different results depending on the initialized velocity field. When the RKE model is initialized with zero-velocity, it yields significantly more mixing between the flow leading up to the fuel assemblies ($2.15 \leq Y/D \leq 2.4$) than when it is initialized with $V = V_\infty$. This is intriguing, because it could potentially hint at a need to understand the transient behavior of the flow. It is important to note that adjustments in the relaxation factors for the zero-velocity initialized RKE model did not notably affect the predicted flow evolution, but lower relaxation factors were needed for the $V = V_\infty$ initialized RKE model to converge on a solution.

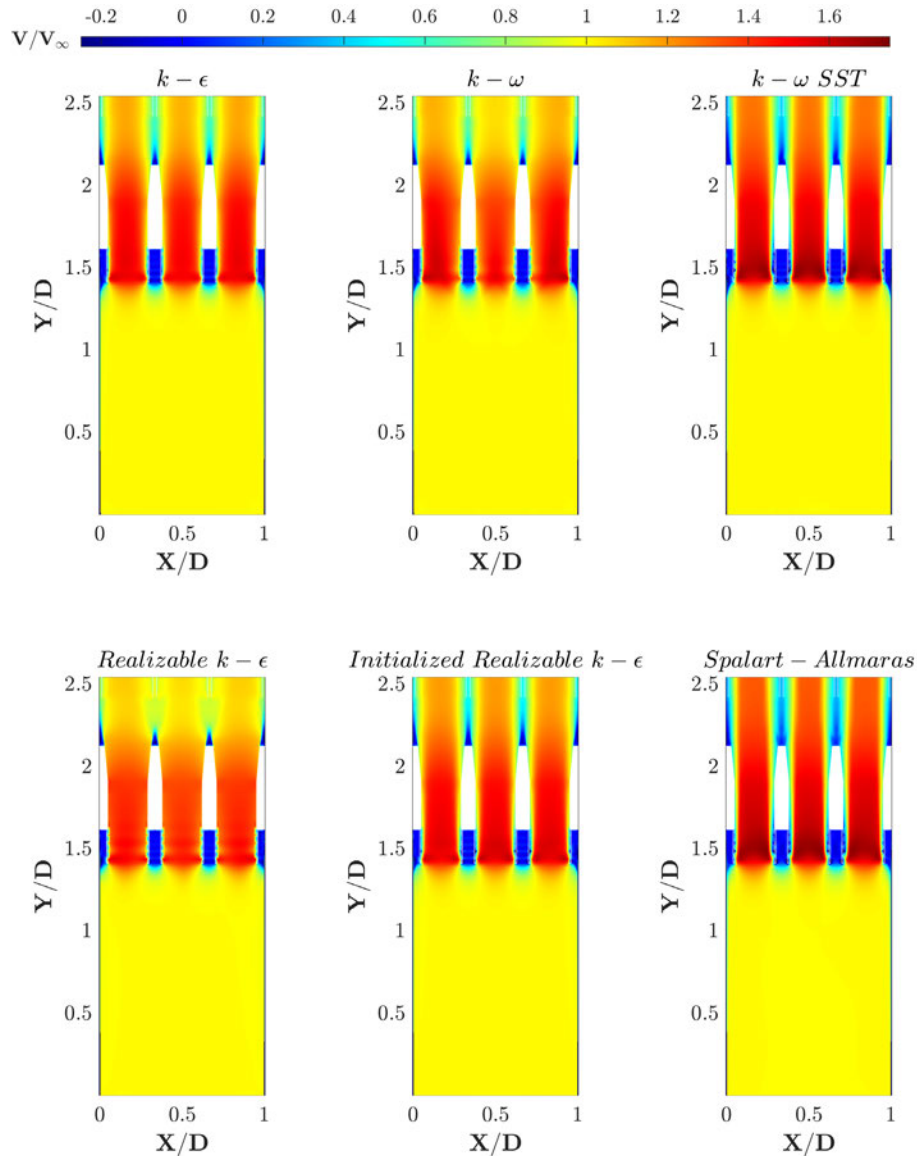


Figure 4. The V/V_∞ field for each investigated model.

A more quantitative understanding can be obtained from Figure 5, where the models are seen to be almost identical until the flow reaches the separation through the legs of the lower grid plate, where the $Y/D \approx 1.5$ profile shows deviations between the models directly downstream of the separation. The variation between the models continues through the top of the geometry directly upstream of the active height at $Y/D \approx 2.5$. It's interesting to point out that the SST and SA models are closely related throughout the flow's evolution, where the most notable difference is seen directly upstream of the active height, where the SA model slightly overpredicts the V/V_∞ relative to the SST model. The un-initialized RKE model shows the lowest velocities upstream of the active height, which is likely due to the increased mixing that the model is predicting in this intermediate mixing region ($2.15 \leq Y/D \leq 2.4$). Note that all RANS models predict different V/V_∞ directly upstream of the active region, which signifies the importance of conducting a validation or using a validated higher fidelity turbulence model as a reference in future works.

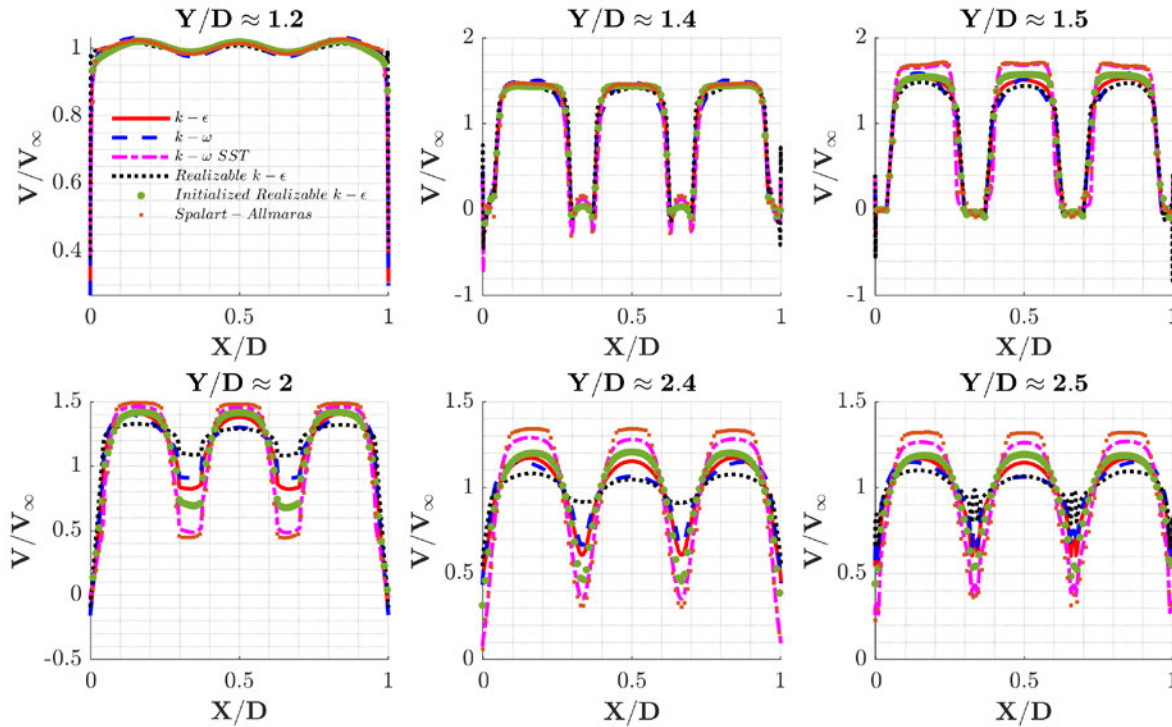


Figure 5. The V/V_∞ spanwise profiles for each investigated model and each streamwise location.

3.2. Spanwise Velocity

Figure 6 demonstrates the U/V_∞ fields for each of the models. All models predict that the most significant recirculation zones occur at the bottom edge of the legs where the flow experiences separation into each of the rectangular legs. This demonstrates that further mesh refinement at this point of separation is likely beneficial to capture the multi-scale motion at those spots. Qualitatively, the models seem identical, however closer inspection reveals significant variations in the intermediate mixing region, particularly with $k-\omega$, the SST model and the zero-velocity initialized RKE model. All three of those models yield higher U/V_∞ than the others in the intermediate mixing region, and they are therefore predicting increased mixing in that region. The presence of two shear layers surrounding the flow exiting the central leg could yield undesirably reduced velocities for the central fuel assembly, and those three models hint at that being the case. This is evidenced with relatively larger spanwise velocities due to the slowing down of the flows, yielding smaller recirculation pockets at the interface between the flows exiting each of the legs. This is a phenomenon that is reported in literature for similar flows [6], and it is worthy of future investigations with a validated model or experiment.

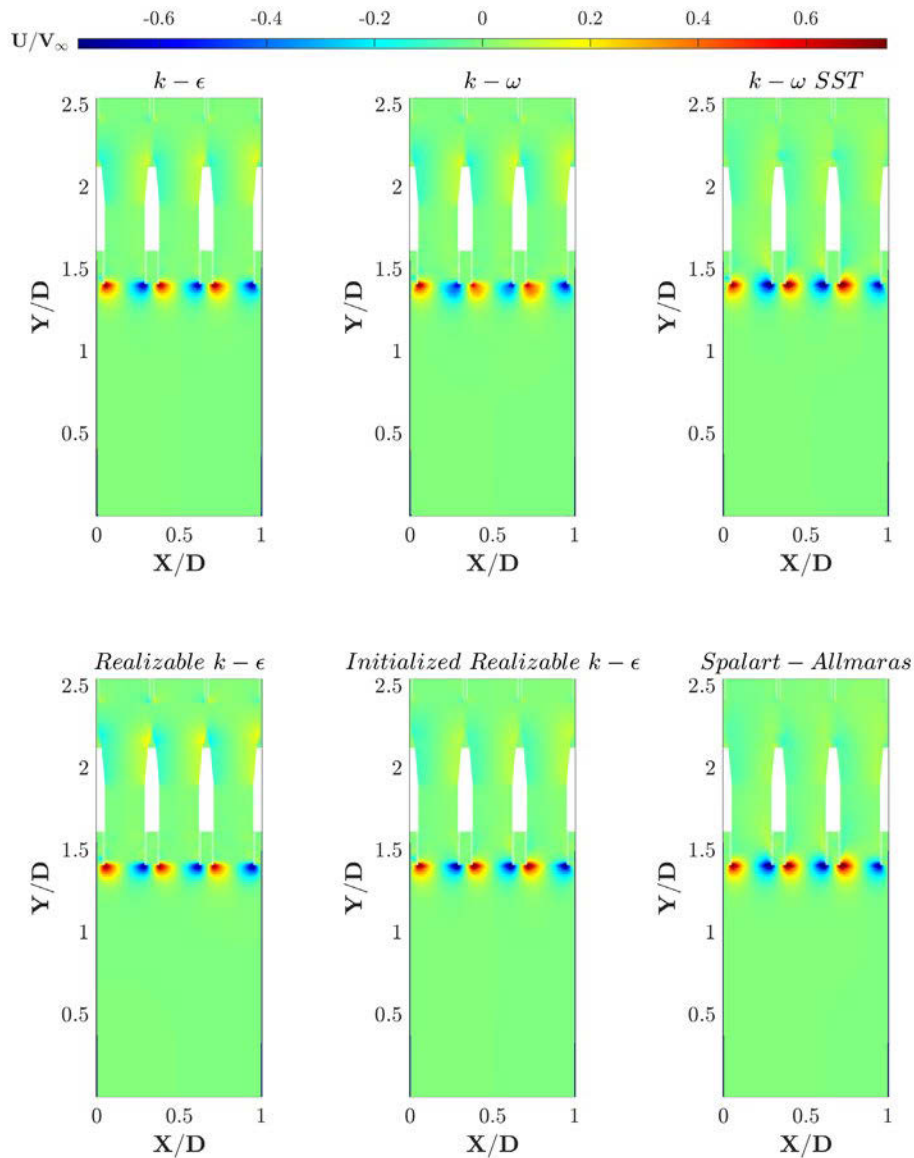


Figure 6. The U/V_∞ field for each investigated model.

The spanwise profiles in Figure 7 show nearly perfect agreement between the models at the start of separation ($Y/D \approx 1.4$), and throughout the legs, which likely demonstrates that this separation phenomenon is insensitive to the RANS turbulence model and may not require a detailed validation in future works. The disagreements start as the flows get closer to the intermediate mixing region, and they increase as the flow progresses further downstream until reaching the top of the simulated geometry directly upstream of the active height. Significant deviations can be observed between the flows, which can exceed 100% difference for certain points such as $X/D \approx 0.9$, where the U/V_∞ predicted by the SA model varies by $\sim 130\%$ relative to the one predicted by the $k-\omega$ model. This signifies a need to have a validated model or experimental reference data for quantifying the behavior in the intermediate mixing region.

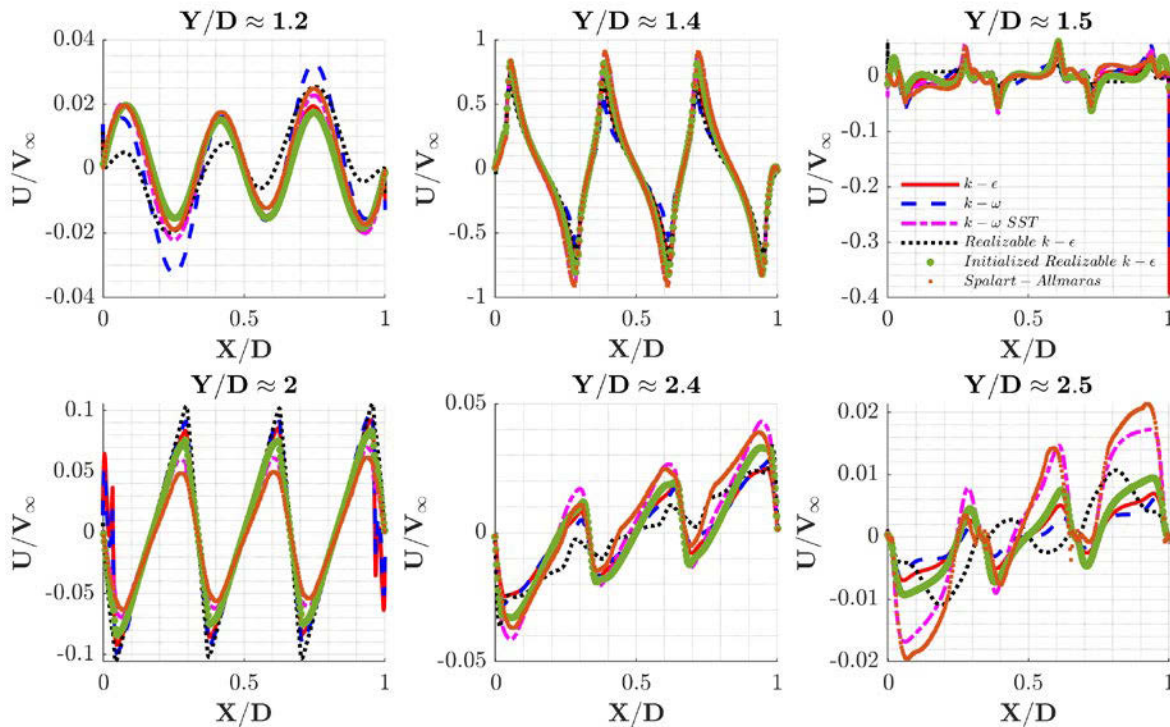


Figure 7. The U/V_∞ spanwise profiles for each investigated model and each streamwise location.

3.3. Pressure

The C_p fields for each of the investigated models can be seen in Figure 8. Once again, the zero-velocity initialized RKE model seems to predict notably different field than the rest. In the absence of a validation or reference validation data, the authors are tempted to regard the zero-velocity initialized RKE model as erroneous; however, a transient analysis will likely clarify that concern. Large pressure gradients are seen at the entrance and exit of the legs. These are the regions with the most complex flow behavior throughout the geometry. An interesting observation is the notable lack of pressure gradients between the flows in the intermediate mixing region, which should be present in situations with parallel flows [7]. It's interesting to point out that all fields (C_p , U/V_∞ , V/V_∞) show roughly no change until roughly 1 hydraulic diameter from the legs ($Y/D \approx 0.4$). This is relevant because it enables an understanding of how much of the domain upstream is needed to accurately capture the flow behavior throughout the rest of the geometry. Like the V/V_∞ fields, the SST and SA models show very close agreement in their C_p predictions throughout the geometry, particularly further downstream. This is relevant when considering potential computational cost savings in future CFD investigations.

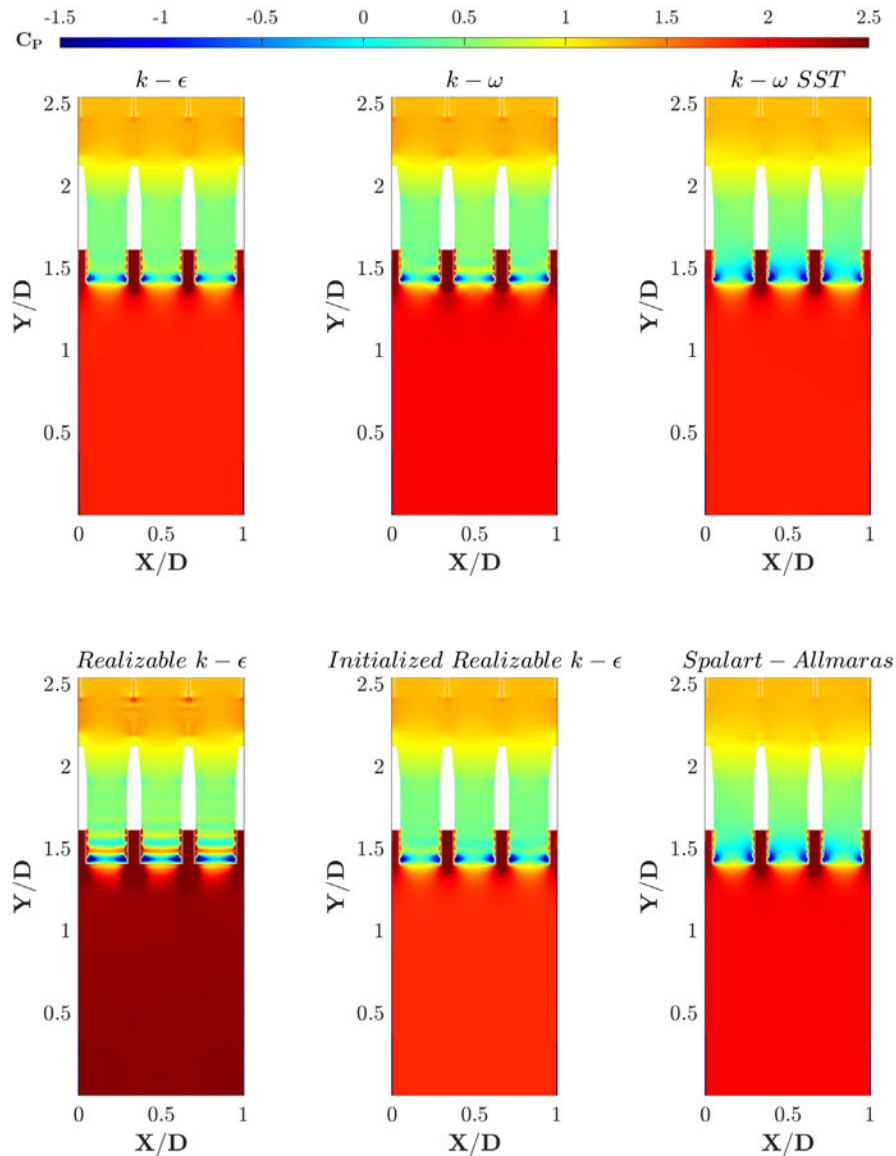


Figure 8. The C_p field for each investigated model.

The spanwise profiles in Figure 9 more closely demonstrate the disagreements between the models. Other than the zero-velocity initialized RKE model, the $k-\omega$ model shows considerable deviation from all the other models at the point of separation ($Y/D \approx 1.4$). This $k-\omega$ deviation continues directly downstream of the separation, where other models like the SST and SA models begin to show variations as well. For the $k-\omega$ model, the greatest deviation around the point of separation is in the recirculation zones between the legs, whereas the SA and SST models show notably lower C_p in the bulk flow of each of the legs. Further downstream in the legs, all models appear to collapse together into a nearly identical flat C_p profile as evidenced by the $Y/D \approx 2$ profiles in Figure 9. Even though there is near perfect agreement upstream of the mixing, the profiles in the intermediate mixing region and further downstream are completely different depending on the model utilized. This further emphasizes the need of validation data for the parallel flows mixing phenomenon experienced in the intermediate mixing region, which will be the subject of future works.

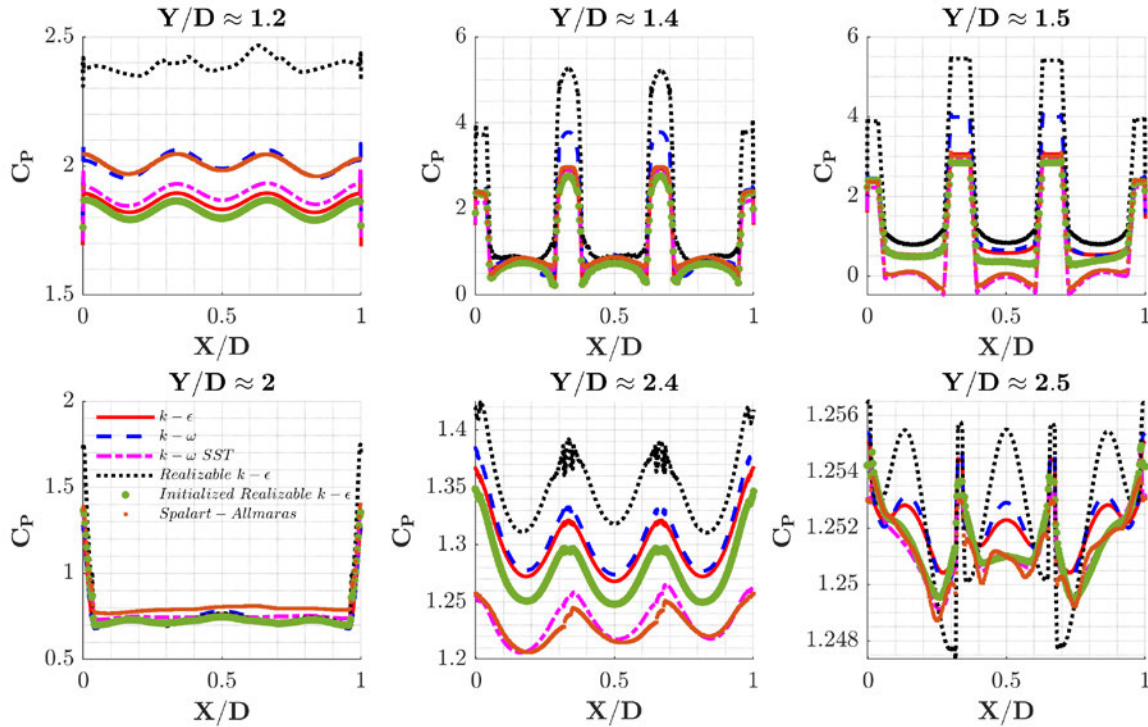


Figure 9. The C_p spanwise profiles for each investigated model and each streamwise location.

4. CONCLUSIONS

The 2-dimensional representation of the inlet region of the NNS is simulated with five different RANS turbulence models in OpenFOAM code, which demonstrated the variability in the resulting velocity and pressure fields due to variations in the RANS turbulence models. All models were found to converge on a consistent solution with or without a bulk velocity initialization except for the RKE model, which yielded different results depending on whether the field was initialized with bulk velocity or zero-velocity. The variation in the RKE model prediction due to initialization options may yield some concerns regarding the transient evolution of the flow. As a summary, Table IV list relevant statistics to quantitatively compare the variability between the models for each of the discussed computed parameters including an average (μ) and the standard deviation (σ) between the models' minimum and maximum values. Future works will investigate the flow's transient behavior, code comparisons, and a validation of the mixing phenomenon.

Table IV. The variation of relevant velocimetric variables in each investigated model.

Model	V/V_∞		U/V_∞		C_p	
	min	max	min	max	min	max
$k-\epsilon$	-0.447	3.325	-0.970	12.697	-6.331	3.322
$k-\omega$	-0.543	2.416	-1.037	10.250	-6.889	4.287
$k-\omega$ SST	-0.969	1.709	-1.030	1.030	-2.157	3.075
Realizable $k-\epsilon$ ($V = 0$)	-0.580	1.555	-0.967	0.972	-3.540	5.976
Realizable $k-\epsilon$ ($V = V_\infty$)	-0.805	1.617	-1.016	1.007	-2.718	3.180
Spalart-Allmaras	-1.008	1.726	-1.026	1.063	-2.054	3.211
Average (μ)	-0.725	2.058	-1.008	4.503	-3.948	3.842
σ/μ (%)	-32.48%	33.75%	-3.07%	121.13%	-54.09%	29.55%

ACKNOWLEDGEMENTS

The authors would like to acknowledge helpful discussions with Dr. DongHun Yeo from the Engineering Laboratory at NIST, and Dr. Lap-Yan Cheng from Brookhaven National Laboratory. The identification of any commercial item in this paper does not imply recommendation or endorsement by the authors or by NIST. Contributions of NIST are not subject to copyright in the United States.

REFERENCES

1. D. Şahin, et al., “NIST Neutron Source Preconceptual Design”, In *RERTR 2022 – 42nd International Meeting on Reduced Enrichment for Research and Test Reactors*, October 3-5 (2022).
2. I.R. Baroukh, A. Gurgun, J.S. Shen, A.G. Weiss, “A Preliminary Thermal-hydraulics Analysis for the NIST Neutron Source”, *Transactions of the American Nuclear Society*, ANS Winter Meeting, November 13-17 (2022).
3. A.G. Weiss, A. Gurgun, I.R. Baroukh, J. Shen, “Sensitivity Analyses of the Thermal-hydraulics Safety Margins in the Proposed NIST Neutron Source Design”, In *Proceedings of the 30th International Conference on Nuclear Engineering*, Kyoto, Japan, May 21-26 (2023).
4. Baroukh, I.R., Gurgun, A., Shen, J.S., Weiss, A.G., “Preliminary CFD Investigations for the NIST Neutron Source”, *Transactions of the American Nuclear Society*, ANS Winter Meeting, November 13-17 (2022).
5. H. G. Weller, G. Tabor, H. Jasak, C. Fureby, “A Tensorial Approach to Computational Continuum Mechanics Using Object-Oriented Techniques,” *Computers in Physics*, **12**(6), pp. 620–631 (1998).
6. A.G. Weiss, P.J. Kristo, J.R. Gonzalez, M.L. Kimber, “Flow regime and Reynolds number variation effects on the mixing behavior of parallel flows”, *Experimental Thermal and Fluid Science*, **134**, 110619 (2022).
7. J. Shen, A.G. Weiss, A. Gurgun, I.R. Baroukh, “A Turbulence Model Sensitivity Analysis of Thermal-hydraulic Properties on the Pre-conceptual NIST Neutron Source”, In *Proceedings of the 30th International Conference on Nuclear Engineering*, Kyoto, Japan, May 21-26 (2023).
8. J. Boussinesq, “Essai sur la théorie des eaux courantes”, *Mémoires présentés par divers savants à l'Académie des Sciences* **23**(1), pp. 1-680 (1877).
9. F.G. Schmitt, “About Boussinesq’s turbulent viscosity hypothesis: historical remarks and a direct evaluation of its validity”, *Comptes Rendus Mécanique* **335**(9-10): 617-627 (2007).
10. B.E. Launder, B.I. Sharma, “Application of the Energy Dissipation Model of Turbulence to the Calculation of Flow Near a Spinning Disc”, *Letters in Heat and Mass Transfer* **1**(2): 131-138 (1974).
11. D.C. Wilcox, “Re-assessment of the scal-determining equation for advanced turbulence models”, *AIAA Journal* **26**(11): 1299-1310 (1988).
12. P.R. Spalart, S.R. Allmaras, “A One-Equation Turbulence Model for Aerodynamic Flows”, In *30th Aerospace Sciences Meeting and Exhibit*, p. 439 (1992).
13. J. Dacles-Mariani, G.G. Zilliac, J.S. Chow, P. Bradshaw, “Numerical/Experimental Study of a Wingtip Vortex in the Near Field”, *AIAA Journal* **33**(9): 1561-1568 (1995).
14. F.R. Menter, “Two-Equation Eddy-Viscosity Turbulence Models for Engineering Applications”, *AIAA Journal* **32**(8): 1598-1605 (1994).
15. T.H. Shih, W.W. Liou, A. Shabbir, Z. Yang, J. Zhu, “A New k- ϵ Eddy Viscosity Model for High Reynolds Number Turbulent Flows”, *Computers & Fluids* **24**(3): 227-238 (1995).
16. D.A. Johnson, L.S. King, “A Mathematically Simple Turbulence Closure Model for Attached and Separated Turbulent Boundary Layers”, *AIAA Journal* **23**(11): 1684-1692 (1985).
17. A.D. Fradeneck, M.L. Kimber, “Applicability of Common RANS Models for the Calculation of Transient Forced to Natural Convection”, *Journal of Verification, Validation and Uncertainty Quantification* **5**(2), p. 021003 (2020).
18. T.H. Shih, J. Zhu, J.L. Lumley, “A New Reynolds Stress Algebraic Equation Model”, NASA Technical Memorandum 106644 (1994).